ISPRS Journal of Photogrammetry and Remote Sensing 141 (2018) 30–45

Contents lists available at ScienceDirect

ISPRS Journal of Photogrammetry and Remote Sensing

journal homepage: www.elsevier.com/locate/isprsjprs

A two-step framework for reconstructing remotely sensed land surface temperatures contaminated by cloud

Chao Zeng[a], Di Long[b,*], Huanfeng Shen[a,c], Penghai Wu[d], Yaokui Cui[b], Yang Hong[b,e,*]

[a] School of Resource and Environmental Sciences, Wuhan University, Wuhan, China
[b] State Key Laboratory of Hydroscience and Engineering, Department of Hydraulic Engineering, Tsinghua University, Beijing, China
[c] Collaborative Innovation Center for Geospatial Information Technology, China
[d] School of Resources and Environmental Engineering, Anhui University, Hefei, China
[e] Department of Civil Engineering and Environmental Science, University of Oklahoma, Norman, OK, United States

ARTICLE INFO

Article history:
Received 26 December 2017
Received in revised form 10 April 2018
Accepted 17 April 2018

Keywords:
Land surface temperature
Reconstruction
Multi-temporal information
Surface energy balance
MODIS

ABSTRACT

Land surface temperature (LST) is one of the most important parameters in land surface processes. Although satellite-derived LST can provide valuable information, the value is often limited by cloud contamination. In this paper, a two-step satellite-derived LST reconstruction framework is proposed. First, a multi-temporal reconstruction algorithm is introduced to recover invalid LST values using multiple LST images with reference to corresponding remotely sensed vegetation index. Then, all cloud-contaminated areas are temporally filled with hypothetical clear-sky LST values. Second, a surface energy balance equation-based procedure is used to correct for the filled values. With shortwave irradiation data, the clear-sky LST is corrected to the real LST under cloudy conditions. A series of experiments have been performed to demonstrate the effectiveness of the developed approach. Quantitative evaluation results indicate that the proposed method can recover LST in different surface types with mean average errors in 3–6 K. The experiments also indicate that the time interval between the multi-temporal LST images has a greater impact on the results than the size of the contaminated area.

1. Introduction

Land surface temperature (LST) is of primary importance in understanding global environment change, urban climatology, and land-atmosphere energy exchange (Kustas and Anderson, 2009; Weng, 2009; Weng and Fu, 2014; Estoque and Murayama, 2017; Zhang and Li, 2018). LST observations are therefore widely used in a variety of fields, including hydrology, meteorology, climate change, vegetation ecology, environmental monitoring, and military reconnaissance (Anderson et al., 2008; Arnfield, 2003; Hansen et al., 2010; Shen et al., 2016). Given the complexity of surface temperatures over land, ground stations cannot provide spatially consistent and temporally continuous measurements over large areas. Satellite remote sensing offers the only possibility for observing LST over the entire globe with acceptable temporal resolution and completely spatial coverage (Li et al., 2013). Satellite-based LST is often retrieved using thermal infrared (TIR) data with the generalized split-window algorithm (Jimenez-Munoz and Sobrino, 2003; Qin et al., 2001; Wan and Dozier, 1996). However, like all the other TIR data-based retrieval methods, the generalized split-window algorithm can only work well when the data are acquired under clear-sky conditions. When solar radiation is obstructed by cloud and/or impacted by other atmospheric disturbances, the retrieval of LST will be greatly affected. As a result, in LST images, only clear-sky pixels have useable information, whereas cloud-covered regions are filled with invalid values (Rajasekar and Weng, 2009). As completely cloud-free weather is rare, especially in rainy seasons or in humid regions, most LST images are contaminated by cloud. Cloud contamination, therefore, greatly limits the subsequent applications of satellite-derived LST in related fields (Yoo et al., 2018).

It has been found that reconstruction techniques can effectively recover missing information and improve the usability of the deteriorated LST. A number of methods have been developed, which can be generally divided into three types according to the sources of reference information: (1) spatial information, (2) multi-temporal observations, and (3) other complementary data, for

---

[*] Corresponding authors at: State Key Laboratory of Hydroscience and Engineering, Department of Hydraulic Engineering, Tsinghua University, Beijing, China.

E-mail addresses: dlong@tsinghua.edu.cn (D. Long), hongyang@tsinghua.edu.cn (Y. Hong).

https://doi.org/10.1016/j.isprsjprs.2018.04.005

example, from ground meteorological stations. The basic spatial information-based methods are spatial interpolation approaches, including inverse distance weighting, spline function and geostatistical interpolation methods. Some studies have attempted to take more factors into account using some multi-variable interpolation methods, such as cokriging (Cai et al., 2009; Ke et al., 2011; Neteler, 2010). As only limited spatial information is referred, the reconstructed regions are often blurred resulting in unsatisfied accuracy. A spectral angle distance weighting reconstruction method has been explored (Shuai et al., 2014). The property of the land surface is quantitatively considered in this study by calculating the spectral angle of original multispectral images. The temporal information-based methods have also been well developed. Reconstruction methods based on time domain analysis have also been developed (Xu and Shen, 2013). The temporal filtering methods, like harmonic analysis, often work well for regions with frequent and dense cloud cover. However, extreme LST values may not be well reconstructed due to the smoothing effect of low-pass filtering. Zeng et al. (2015) filled invalid LST values using a multi-temporal classification and a robust temporal regression. Compared with the temporal filtering approach, the method can fill invalid LST values accurately with much less reference data.

It should be noted that the aforementioned methods can only provide hypothetical clear-sky LST values, but not the real LST under cloudy conditions. In general, during daytime the cloud-covered LST is lower than the cloud-free LST because the land surface receiving solar radiation is hidden by cloud. For the third type of reconstruction methods, other land surface information is incorporated to estimate the real LST. Jin (2000) proposed a neighboring-pixel (NP) approach to reconstruct the LST of cloudy pixels based on the surface energy balance. In this approach, the LST of cloudy pixels is interpolated from the neighboring clear pixels surrounding the cloudy pixels. In addition, surface wind and air temperature are also incorporated. Based on Jin's approach, a temporal NP method was developed to estimate cloudy LST pixels from geostationary satellites (Lu et al., 2011). Then, a spatially and temporally NP method was also proposed to reconstruct cloud-contaminated pixels in daily MODIS LST products (Yu et al., 2014). Since the surface energy balance is considered, the NP-based method can reconstruct the real LST for cloudy pixels. However, for these methods, ground-based measurements are often needed to calculate regional parameters, which makes them difficult to implement for ungauged or poorly gauged regions.

With the development of the above methods, the usability of satellite-derived LST has been greatly improved. However, these methods all have their advantages and limitations under different circumstances. In general, the temporal information-based methods are more effective, but the real LST cannot be obtained. The surface energy balance-based methods are more accurate, but the parameters are difficult to obtain. The overall objective of this study is therefore to develop a new flexible and effective method for cloud-contaminated LST reconstruction. The advantage of the newly developed approach is that it can generate more accurate LST for cloudy pixels, without depending largely on ground-based ancillary data. This approach makes satellite-based LST observations more applicable to large areas, and should be valuable in meteorological and hydrological studies and applications. In the following sections, we first describe the algorithm, and then demonstrate its performance based on both simulated and actual experiments.

2. Method

As shown in the flowchart of Fig. 1, first, a multi-temporal reconstruction process is employed to obtain the ideal clear-sky LST for the cloud-contaminated region in combination with the Normalized Difference Vegetation Index (NDVI). Second, a surface energy balance (SEB) equation-based method is used to correct the clear-sky LST to the real LST with surface shortwave radiation information. And the results are verified using SURFace RADiation (SURFRAD) ground measurements.

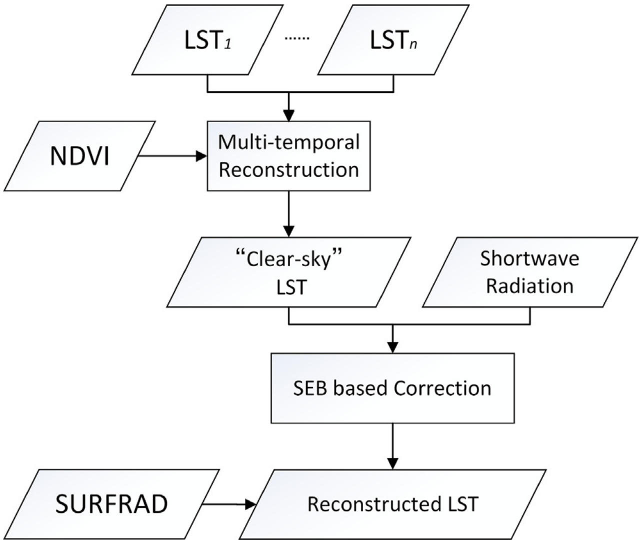

Fig. 1. Flowchart of the proposed two-step framework for LST reconstruction.

2.1. Multi-temporal reconstruction

In the first step, a multi-temporal reconstruction method was introduced to obtain the clear-sky land surface temperature. It has been shown that two LST maps acquired during a short period change linearly for the same type of feature (Zeng et al., 2015). Therefore, the contaminated LST can be reconstructed by the LST acquired at another time:

$$T_{s0} = a \cdot T_{s0}' + b \tag{1}$$

where $T_{s0}$is the LST to be recovered, $T_{s0}'$is the reference LST acquired at a near time for T_{s0}, and a and b are regression coefficients. Since pixels with the similar land surface property have similar trends in LST change, the regression coefficients a and b can be calculated by the similar common pixels (common pixels are referred to as the pixels with valid values in both LST images) of the contaminated LST image and the reference LST image. The procedures are shown in Fig. 2.

It has also been found that LST has a strong relationship with the vegetation index (VI) (Amiri et al., 2009, Dousset and Gourmelon, 2003; Jin and Dickinson, 2010; Schultz and Halpert, 1995). A hypothesis is therefore proposed here: during a period, the change of LST is related to vegetation index values. To test this hypothesis, an example is shown in Fig. 3. Two MODIS LST images acquired on January 1, 2010, and January 5, 2010 are shown in Fig. 3(a). The difference map between the two LST images is shown in Fig. 3(b). The corresponding NDVI map for the same area is shown in Fig. 3(c). Fig. 3(d) shows the scatterplot of the temperature difference against NDVI. The distribution of the black dots indicates a strong relationship between the temperature difference and NDVI, showing a correlation coefficient (R) of 0.666.

Therefore, the VI could also be involved in the calculation of the regression coefficients in Eq. (1). Since VI values often remain constant in a short term, multi-day composite VI can be used for convenience. In this paper, an adaptive determination procedure for the similar pixel selection was employed (Zeng et al., 2013). In

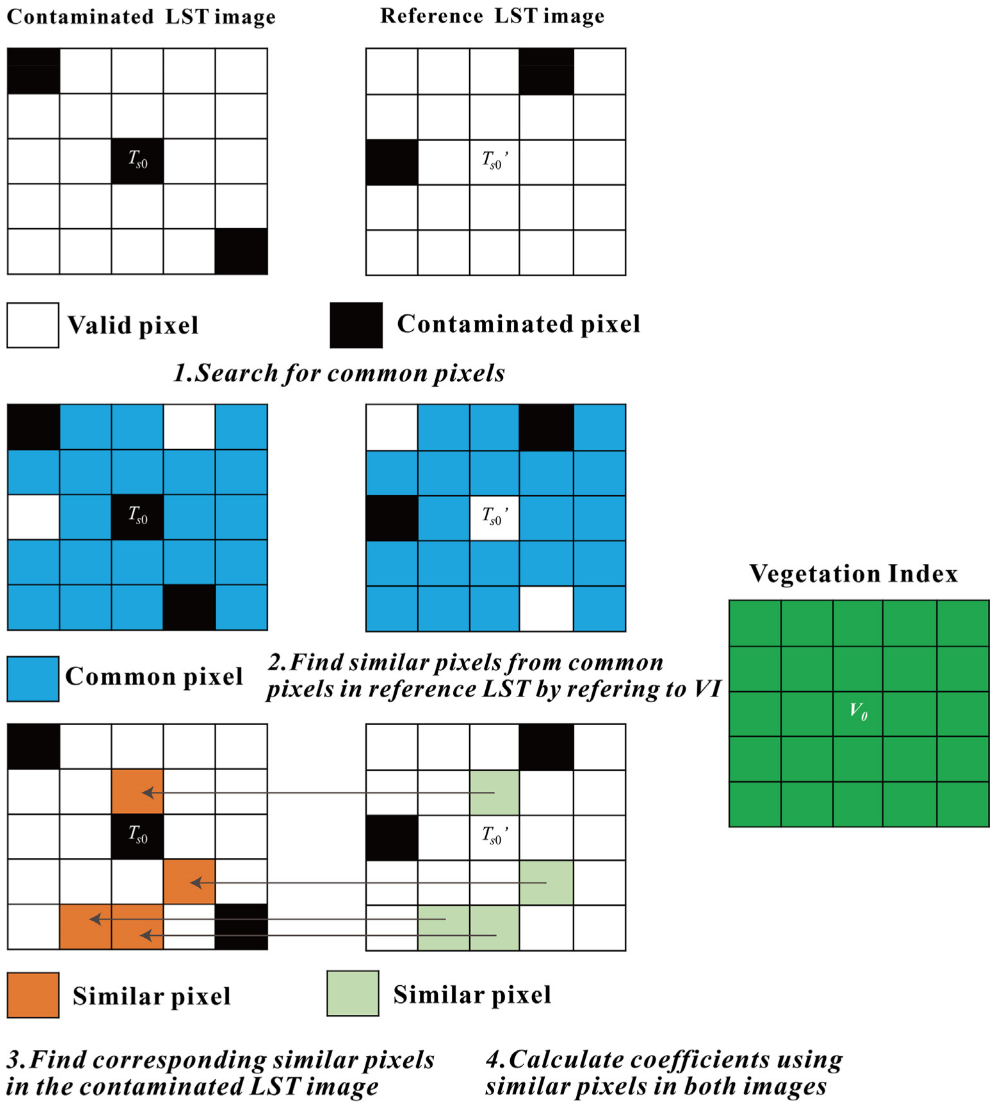

Fig. 2. Procedures of searching for similar common pixels from both the contaminated LST images and reference LST image for calculating regression coefficients *a* and *b* in Eq. (1).

the reference LST image, similar pixels are searched from the common pixels using the following constraints:

$$\left|T_{s0}' - T_{si}'\right| \leqslant T_{thd} \tag{2}$$

$$|V_0 - V_i| \leqslant V_{thd} \tag{3}$$

where $T_{si}'$is the LST for the pixel near the pixel withT_{s0}', $V_i$and $V_0$are the corresponding VI values, T_{thd} and V_{thd} are the threshold values of LST and VI, respectively. The thresholds represent the local similarity related to the smoothness of adjacent areas (e.g., 5 × 5 pixels). In this study, they are adaptively calculated by the local standard variation:

$$T_{thd} = \sqrt{\frac{1}{n}\sum_{i=1}^{n}\left(T_{si}' - \overline{T}_s'\right)^2} \tag{4}$$

$$V_{thd} = \sqrt{\frac{1}{n}\sum_{i=1}^{n}(V_i - \overline{V})^2} \tag{5}$$

where *n* is the total number of valid pixels in the adjacent areas. The local standard variation can represent the smoothness of the area. Therefore, the constraints would be smaller for homogeneous surface to select the most similar pixels. But it would also be effective in searching for similar pixels for heterogeneous surfaces without being greatly affected by noise in images. For serious cloud-contaminated situations, not enough pixels can be found in a small region. In this situation, a maximum threshold value will be assigned (e.g., 0.05). After determining the similarity thresholds, the similar pixels of center pixel can then be selected. In this procedure, an adaptive searching window centered on each contaminated pixel is used to select the similar pixels. First, an initial and a maximum window size and the desired number of the similar pixels are set (e.g., 11 × 11 pixels). For each contaminated pixel, all the common pixels of the contaminated LST image and reference LST image located in the window are set as candidates. Then Eqs. (2) and (3) are implemented. If the desired number of similar pixels (e.g., 20) is not satisfied, the window size will be enlarged until the maximum size has been reached.

When all the similar pixels in the window have been identified, the coefficients can then be calculated with Eq. (1). Considering that the contributions of each pixel vary due to differences in land surface property and spatial location, a weighted linear regression method is employed here. A synthetic difference index is employed to calculate the weight:

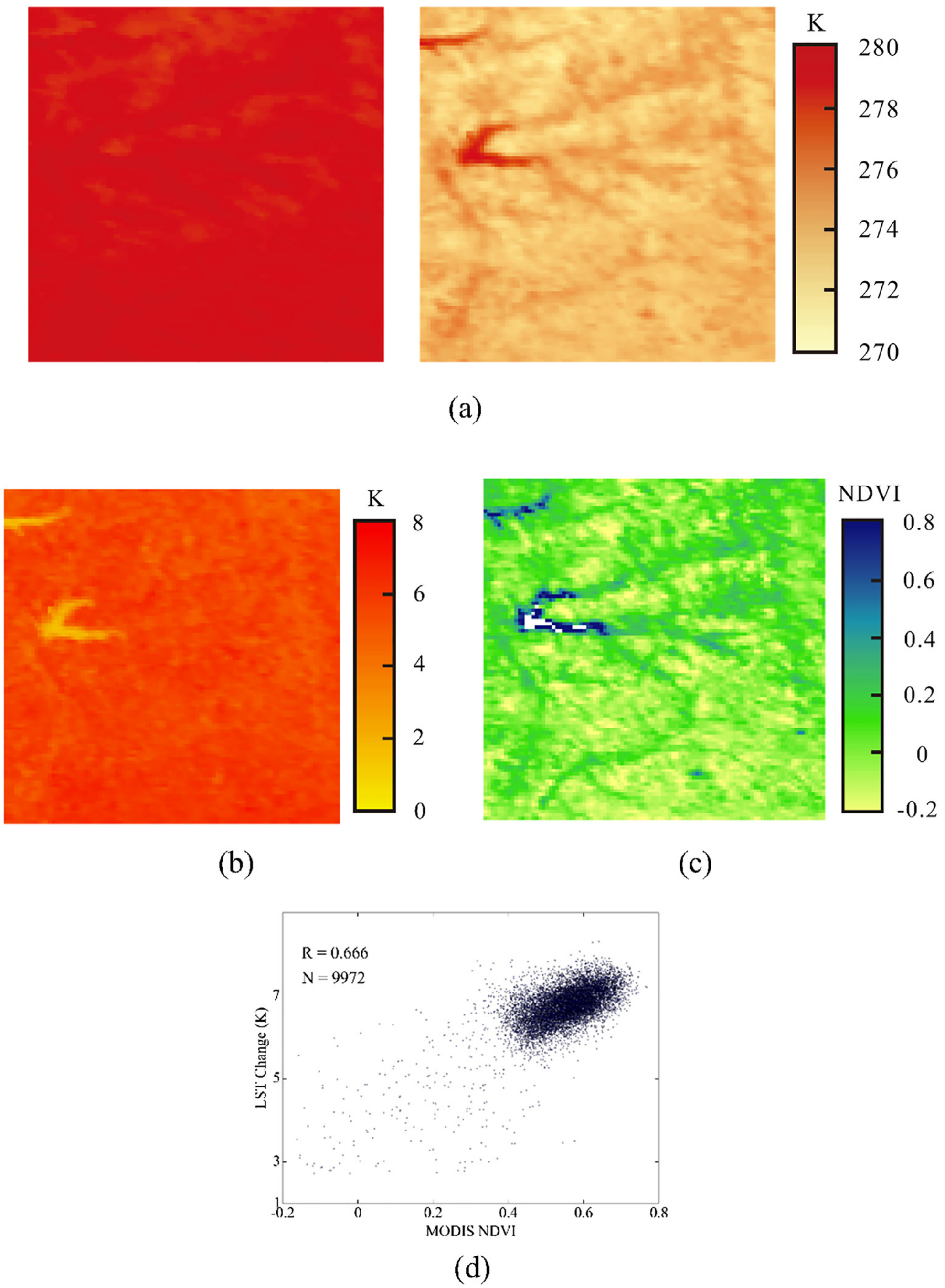

Fig. 3. An example of the relationship between NDVI and LST: MODIS LST acquired on (a) January 1 and January 5, 2010, (b) the LST difference between the two dates, (c) the corresponding 16-day composite NDVI distribution for the period, and (d) the scatterplot of (b) and (c).

$$D_i = |T_{s0}' - T_{si}' + \xi| \cdot |V_0 - V_i + \xi| \cdot \left((x_i - x_0)^2 + (y_i - y_0)^2\right) \qquad (6)$$

where x_i, y_i, x_0 and y_0 represent the locations of the similar pixel and contaminated pixel, and ξ is a small value to ensure that D_i is not equal to zero (e.g. 0.001). The term $\left((x_i - x_0)^2 + (y_i - y_0)^2\right)$ describes the spatial distance between the corresponding similar pixel and the contaminated pixel in the reference image, and $|T_{s0}' - T_{si}' + \xi| \cdot |V_0 - V_i + \xi|$ represents the difference of land surface property.

For the convenience of calculation, weights of each selected similar pixel are normalized as:

$$W_i = (1/D_i) \,/\, \sum_{i=1}^{m} (1/D_i) \qquad (7)$$

Then the range of weight W_i is normalized from 0 to 1, and the sum of all the weights is 1. Subsequently, the coefficients can be solved by:

$$a = \frac{\sum_{i=1}^{m} W_i (T_{si} - \overline{T}_s)(T_{si}' - \overline{T}_s')}{\sum_{i=1}^{m} W_i (T_{si}' - \overline{T}_s')^2} \qquad (8)$$

and $b = \overline{T}_s - a\overline{T}_s'$ (9)

where $\overline{T}_s$and $\overline{T}_s{}'$are the mean values of all the similar pixels in the searching window on the contaminated and reference LST images, respectively.

Extreme situations that only a few or even no similar pixel could be found after the procedure illustrated above should also be considered. In the case that the number of similar pixels does not meet the desired number (e.g., 20) even the window size reaches the maximum size, but the number is more than 2, the algorithm will still be performed using all the selected similar pixels (minimum number: 3). For the exceptional case when there is no similar pixel for the algorithm, the center pixel will be identified as an outlier. Under this condition, the contaminated pixel value will be adjusted to fit the background. Therefore, the coefficient is simplified as:

$$a = \frac{\overline{T}_s}{\overline{T}_s{}'} \tag{10}$$

$$\text{and } b = 0 \tag{11}$$

2.2. Surface energy balance-based correction

Since cloud may obstruct solar radiation and consequently affect LST, it is necessary to correct the clear-sky LST to the real LST under cloudy conditions:

$$T_{cloud0} = T_{s0} + \Delta T_{s0} \tag{12}$$

where $T_{cloud0}$is the real LST under cloudy conditions and ΔT_{s0} is the correction for T_{s0}, and can be derived using the SEB. In this study, a SEB-based method was employed to address this issue. Over the land surface, the SEB is written as:

$$Q = G + H + LE \tag{13}$$

where Q is the net radiation, G is the ground heat flux, H and LE denote sensible heat flux and latent heat flux, respectively. In daytime, the net radiation can be written as the sum of net shortwave and longwave radiation:

$$Q = S_n - L_n \tag{14}$$

where $\mathrm{S_n}$ is the net shortwave radiation and $\mathrm{L_n}$ is the net longwave radiation.

Then the SEB can be rewritten as:

$$S_n - L_n = G + S_{hle} \tag{15}$$

where $\mathrm{S_{hle}}$ is the sum of sensible heat and latent heat flux. With all the terms in Eq. (15) being partially differentiated with respect to $\mathrm{T_s}$, it can be written as:

$$\frac{\partial S_n}{\partial T_s} - \frac{\partial L_n}{\partial T_s} = \frac{\partial G}{\partial T_s} + \frac{\partial S_{hle}}{\partial T_s} \tag{16}$$

Based on the conventional force-restore method, the ground heat flux can be calculated by Jin (2000) and Jin and Dickinson (2000):

$$G = k_g \frac{\partial T}{\Delta Z} = k_g \frac{T_s - T_d}{\Delta Z} \tag{17}$$

where k_g is the thermal conductivity of the ground soil in units $\mathrm{W\,m^{-1}\,K^{-1}}$; ΔZ is the depth of the subsurface layer; and T_d is the temperature at the subsurface layer. Since the subsurface layer temperature T_d is much less sensitive than skin temperature to surface insolation (Jin, 2000), for two similar pixels, the equation can be written as:

$$\frac{\partial G}{\partial T_s} = \frac{\partial}{\partial T_s}[k_g \frac{T_s - T_d}{\Delta Z}] \approx \frac{k_g}{\Delta Z} \tag{18}$$

Then Eq. (16) can be written as:

$$\Delta T_s = \frac{\Delta Z}{k_g}(\Delta S_n - \Delta L_n - \Delta S_{hle}) = \frac{\Delta Z}{k_g}(1 - p - q)\Delta S_n \tag{19}$$

where $p = \Delta L_n/\Delta S_n$, $q = \Delta S_{hle}/\Delta S_n$, $\Delta \mathrm{S_n}$ is the difference of net shortwave radiation between the two similar pixels. Since ΔL_n and ΔS_{hle} are hard to obtain by remote sensing, empirical approximate relationships can be used (Jin, 2000; Lu et al., 2011; Yu et al., 2014):

$$L_n = p_0 + pS_n \tag{20}$$

$$S_{hle} = q_0 + qS_n \tag{21}$$

where p is a coefficient related to surface soil properties and q is a coefficient related to local surface cover types and soil properties. Given that the net shortwave radiation is defined as the sum of incoming and outgoing shortwave radiation, the net shortwave radiation can be written as:

$$S_n = S_+ - S = (1 - \alpha)S_+ \tag{22}$$

where α is the surface albedo, S_+ and S_- are the incoming and outgoing shortwave radiation, respectively. Then Eq. (19) can be rewritten as:

$$\Delta T_s = c\Delta[(1 - \alpha)S_+] \tag{23}$$

where $c = \Delta Z(1 - p - q)/k_g$.

It can be found that parameter $c$is mainly determined by surface properties. Therefore, it is reasonable to assume that the similar pixels have close values of the parameter. For each pixel with the LST to be reconstructed in the contaminated LST image, the corresponding parameter$c$is calculated by:

$$c = \frac{1}{C_m^2}\sum_{i=1}^{m}\sum_{j=i+1}^{m}(T_{s,i} - T_{s,j})/[(1 - \alpha_i)S_{+i} - (1 - \alpha_j)S_{+j})] \tag{24}$$

where $C_m^2$is combinations of any 2 in m similar pixels, i and j denote the ith and jth similar pixels, respectively. Ultimately, $\Delta \mathrm{T_{s0}}$ can be derived as follows:

$$\Delta T_{s0} = \frac{1}{m}\sum_{i=1}^{m} c[(1 - \alpha_0)S_{+0} - (1 - \alpha_i)S_{+i})] \tag{25}$$

From Eq. (25) it is clear that the LST correction term ΔT_{s0} for T_{s0} is a function of c and albedo reflecting the impact of surface properties and S_+ reflecting the impact of atmospheric disturbance (including cloud contamination) on incoming shortwave radiation for the contaminated pixel.

2.3. Statistical metrics

To evaluate the two steps of the proposed framework, simulated and real experiments were carried out, respectively. In the simulated experiments, an invalid region was simulated in an uncontaminated LST image, and then the reconstructed LST values were compared with the original values. The reconstructed LST values after clear-sky correction were compared with the LST measurements at SURFRAD sites in the real experiments. The experimental results were assessed quantitatively using some statistical metrics. The first one is the Pearson correlation coefficient used to assess the degree of consistency between estimated and observed values. The second index used is the Average Relative Error (ARE), which is used to evaluate the relative error of reconstructed LST values. It can be calculated by:

$$ARE = \left(\sum_{i=1}^{M}(|T_{si} - T_{ri}|/T_{si})\right)/M \times 100\% \tag{26}$$

where M is the total number of contaminated pixels, T_{si} and T_{ri} are original and reconstructed LST of the ith contaminated pixel, respectively. As the former two metrics are dimensionless, the Mean Absolute Error (MAE) was also employed to assess the absolute accuracy.

3. Data

3.1. Satellite data

The proposed method is universal and can be implemented on most satellite-derived LST products. Since MODIS LST is one of the most popular products, the MODIS datasets were used in experiments performed in this study. The MODIS sensors onboard the Terra and Aqua satellites have 36 spectral bands ranging from the visible to the thermal infrared spectrum. The spatial resolution varies from 250 m (bands 1 and 2) to 500 m (bands 3–7) and 1000 m (bands 8–36) (Shen et al., 2011). The MODIS sensors view the entire Earth every 1 or 2 days. The daily level 3 LST product at 1 km spatial resolution (MOD11A1) was used in this study. In addition, the MODIS vegetation index product (MOD13A2), albedo product (MCD43A3), and emissivity product (MOD11B1) were also used. The vegetation index products provide NDVI and EVI at 1 km spatial resolution for each16-day composite period. The albedo products provide 500 m data describing both directional hemispherical reflectance (black-sky albedo) and bihemispherical reflectance (white-sky albedo) every 16 days. The MOD11B1 products provide daily per-pixel temperature and emissivity values at 6 km resolution. The Global LAnd Surface Satellite (GLASS) downward shortwave radiation product (Liang et al., 2013; Zhang et al., 2014) can provide shortwave radiation at 5 km resolution. Since the resolution of the original LST product is approximately 1 km, for the convenience of calculation, all the satellite data were resampled (i.e., nearest neighbor resampling used in the experiments) to the $0.01^\circ \times 0.01^\circ$ resolution in the geographic projection and clipped into 400 × 400 pixel images.

3.2. Surface measurements

Accurate ground-measured LST in different climatic regions is essential to evaluate the reconstruction method. In this study, SURFRAD ground measurements were used. The SURFRAD network

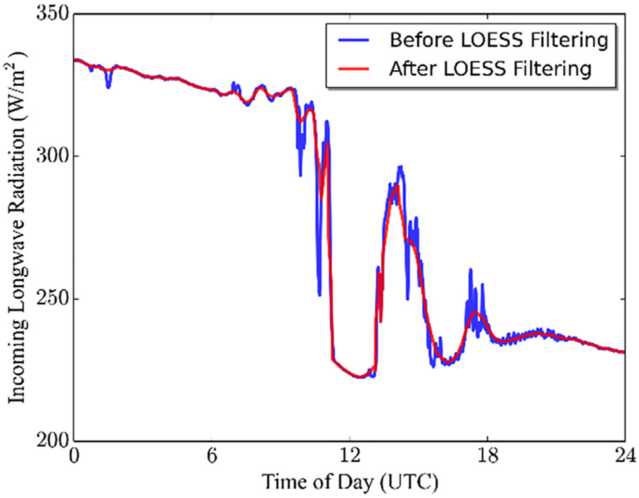

Fig. 5. SURFRAD incoming longwave radiation data acquired from the GWN site on January 1, 2010, before and after the LOESS filtering.

Table 1
Six stations of land surface temperature measurements selected from the SURFRAD network.

Station name	Latitude (°)	Longitude (°)	Altitude (m)	State
Bondville (BON)	40.05	−88.37	213	Illinois
Fort Peck (FPK)	48.31	−105.10	634	Montana
Goodwin Creek (GWN)	34.25	−89.87	98	Mississippi
Table Mountain (TBL)	40.125	−105.237	1689	Colorado
Desert Rock (DRA)	36.624	−116.019	1007	Nevada
Sioux Falls (SXF)	43.73	−96.62	473	South Dakota

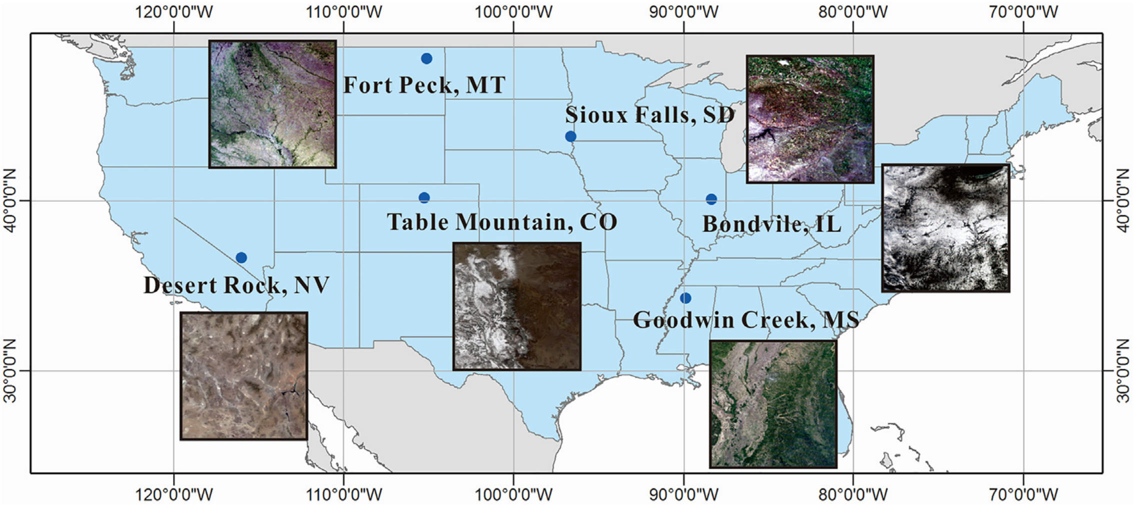

Fig. 4. Six SURFRAD stations and the corresponding true color MODIS images: BON of February 19, DRA of September 11, FPK of July 25, GWN of May 4, SXF of May 29, TBL of March 16, 2010. (For interpretation of the references to colour in this figure legend, the reader is referred to the web version of this article.)

was established in 1993 through the support of NOAA's Office of Global Programs. The primary objective of this project was to support climate research with accurate, continuous, long-term measurements pertaining to the surface radiation budget over the United States (http://www.esrl.noaa.gov/gmd/grad/surfrad/overview.html). The stations provide a set of broadband infrared

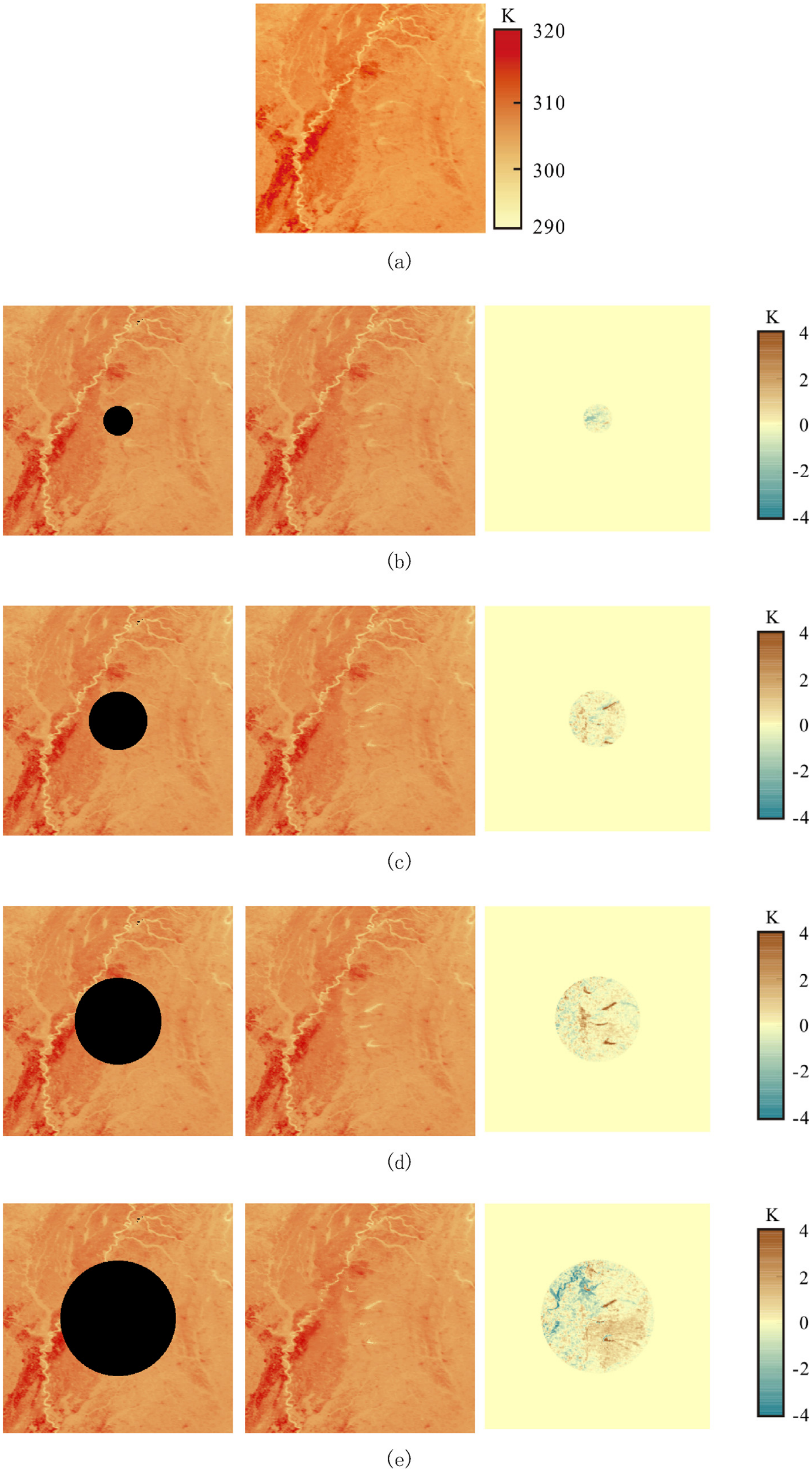

(a)

(b)

(c)

(d)

(e)

Fig. 6. An example of the simulated experiment: (a) the original LST of the study area (GWN) acquired on May 4, 2010, the simulated LST data degraded by the invalid regions with (b) 50, (c) 100, (d) 150, (e) 200 pixel diameter, the corresponding reconstructed LST (second column) and the error maps (third column).

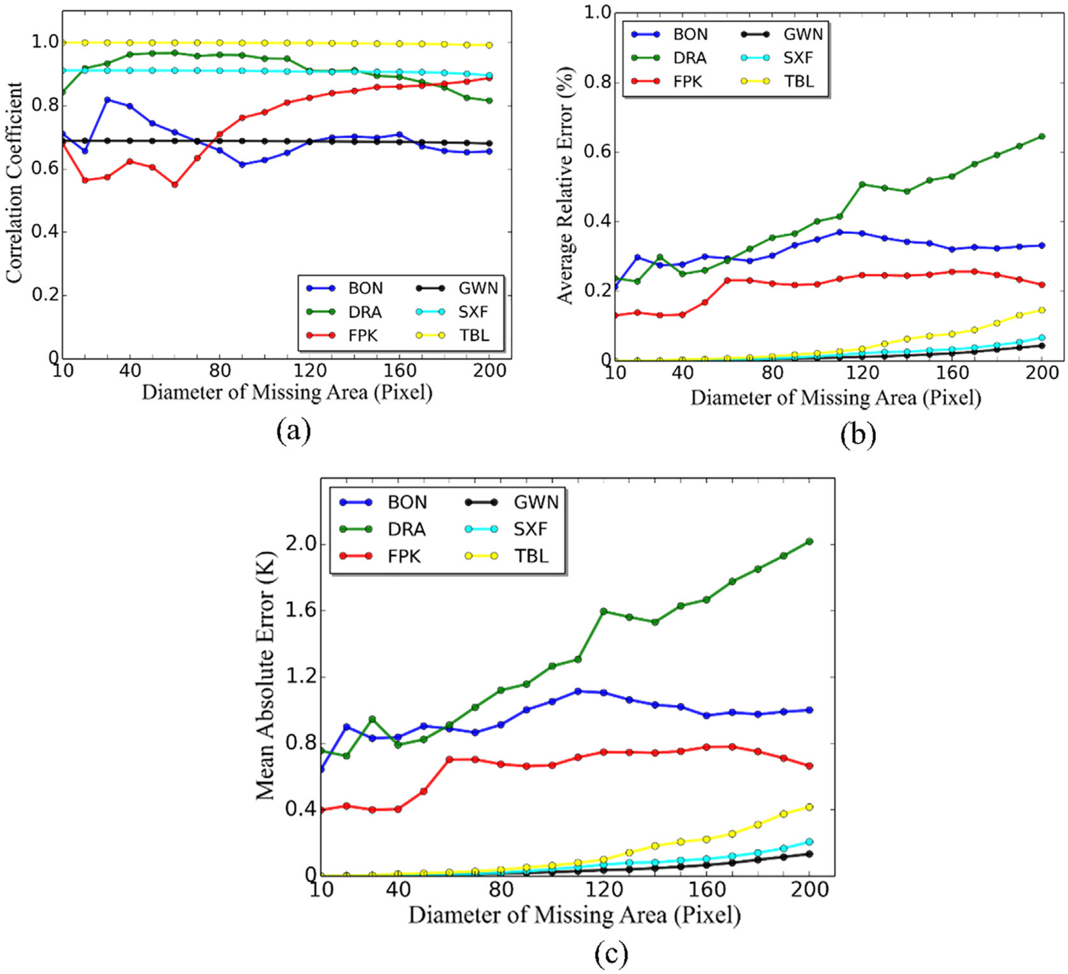

Fig. 7. (a) Correlation coefficients, (b) average relative errors, and (c) mean absolute errors of the 6 experimental regions (BON, DRA, FPK, GWN, SXF, and TBL) with different sizes of missing areas.

surface radiation and meteorological observations every 3 min before 2009 and every 1 min after 2009. Due to the good continuity and high quality of the measurements, the network has been used as the LST ground truth for satellite-derived LST validation (Li et al., 2014; Wang and Liang, 2009). Six SURFRAD sites were used in this study Table 1 and the corresponding true color MODIS images are shown in Fig. 4. The surface types of BON, FPK, GWN and SXF are mostly grasses, crops and few trees. TBL region is covered by sandy with a mix of exposed rocks, sparse grasses, desert shrubs, and small cactus. And the surface of DRA region is made up of fine rock and scattered desert shrubs (Augustine et al., 2010). Therefore, the applicability of proposed framework can be well tested.

However, since noise exists in any observations, a quality control procedure must be implemented before using SURFRAD measurements. In this paper, LOcal regrESSion (LOESS) was employed to perform a temporal filtering on SURFRAD data. LOESS is a very flexible and ideal method to model non-linear processes or provide a smoothing parameter value and the degree of the local polynomial (Cleveland and Devlin, 1988). The basic idea is to create a function that describes the deterministic part of the variation in the data, by fitting simple models to localized subsets of the data with a weight matrix w, which is calculated using a tri-cube weight function:

$$w(u) = \begin{cases} \left(1 - |u|^3\right)^3, & if\,|u| < 1 \\ 0, & if\,|u| \geqslant 1 \end{cases}$$

where u is the normalized distance obtained from the ratio between the actual distance of a point and the maximal distance in a subset. With this approach, the noise in the SURFRAD observations can be filtered. To verify the effect of the LOESS filter, an experiment was carried out using observations from the GWN site on January 1, 2010. Fig. 5 shows a comparison on SURFRAD incoming longwave radiation before (blue[1] line) and after (red line) the LOESS filtering. Before the LOESS filtering, obvious fluctuations can be detected during the whole day. The fluctuations, which were likely to be measurement error or other factors, would reduce the reliability of the ground truth. After the filtering, the noise was mostly removed and the time series became much smoother.

Since only surface radiation instead of direct LST was observed at these stations, a transformation must be implemented to convert SURFRAD radiation to LST. The general way is to convert outgoing and incoming radiation into the surface temperature with broadband emissivity and using the Stefan–Boltzmann law, which can be expressed (Wu et al., 2013, 2015; Niclòs et al., 2018):

$$L_o = \varepsilon_b \cdot \sigma \cdot {T_s}^4 + (1 - \varepsilon_b) \cdot L_i \qquad (28)$$

where L_o is the measured outgoing longwave radiation, ε_b is broadband longwave surface emissivity, σ is the Stefan–Boltzmann constant ($5.67 \times 10^{-8}\,\mathrm{W\,m^{-2}\,K^{-4}}$), T_s is the LST, and L_i is the

---

[1] For interpretation of color in Fig. 5, the reader is referred to the web version of this article.

measured incoming longwave radiation. Then LST can be solved as follows:

$$T_s = \left[\frac{L_o - (1 - \varepsilon_b) \cdot L_i}{\varepsilon_b \cdot \sigma}\right]^{1/4} \tag{29}$$

The broadband emissivity ε_b can be estimated from MODIS narrowband emissivity products using an empirical relationship (Wang et al., 2005):

where ε_{29}, ε_{31}, and ε_{32} are MODIS band 29, 31 and 32 narrowband emissivities, respectively, from global 6 km daily land surface temperature/emissivity data (MOD11B1).

It should also be concerned the uncertainty in comparing in-situ estimated LST with satellite-derived LST. The MODIS sensor can provide LSTs in 1 km resolution, which is much larger than the scope of a land surface site. The SURFRAD sites were chosen to be located in regions with minimal surface heterogeneity. The error source of different scales can therefore be reduced to an acceptable range.

4. Results and discussion

4.1. Different sizes of missing areas

First, the ability of reconstruction for the multi-temporal algorithm for large areas was evaluated. With a larger missing area, less neighborhood information was used in the method, which might introduce more uncertainties to the results. In this experiment, a cloud-free LST image was selected, and then degraded to a cloud-contaminated LST image with different sizes of invalid regions. Then the degraded LST images were reconstructed and assessed relative to the original cloud-free image. As shown in Fig. 6, it can be found that all the reconstructed LST images are highly consistent with the original LST image. Error maps of the reconstructed maps are also shown in Fig. 6. It is showed that as the invalid region expands, the errors become more significant. In Fig. 6(a), while the invalid region is only 50 pixel diameter, the errors are less than 1 K. In Fig. 6(b), some of the errors are about 2 K with an invalid region of 100 pixel diameter. The errors are even more obvious in Fig. 6(c) and (d) with larger invalid regions. It should be noted that some marked patterns can be found in Fig. 6 (b)–(d), which is because the adjoining similar pixels were reconstructed by similar coefficients. As a result, the errors appeared in a regular shape.

To further illustrate the effect of the reconstruction algorithm on different sizes of missing areas, all the experimental areas were tested with cloud-free LST data. The data acquisition dates for the BON, DRA, FPK, GWN, SXF and TBL regions were June 30, September 11, September 28, May 4, May 29 and March 16, 2010, respectively. Quantitative evaluation is shown in Fig. 7. In most cases, the correlation coefficients were larger than 0.7. The correlation coefficients remained generally similar with an expanding size of the invalid region. However, for the FPK region, the correlation coefficients increased obviously with the size of the missing area. It is because the experimental area was relatively homogeneous. As the invalid region expanded, more surrounding pixels were involved in the searching procedure, which made the reconstruction more stable. In Fig. 7 (b) and (c), the AREs of GWN, SXF and TBL were less than 0.2%, and the MAEs were less than 0.5 K. It is therefore indicated that the algorithm is reliable for these test regions. However, for the DRA region, the AREs and MAEs obviously increased with the size of the missing area, though the ARE was still less than 0.7 and the MAE was less than 2 K. The results suggest that the proposed algorithm can recover reliable LST values in homogeneous or heterogeneous regions.

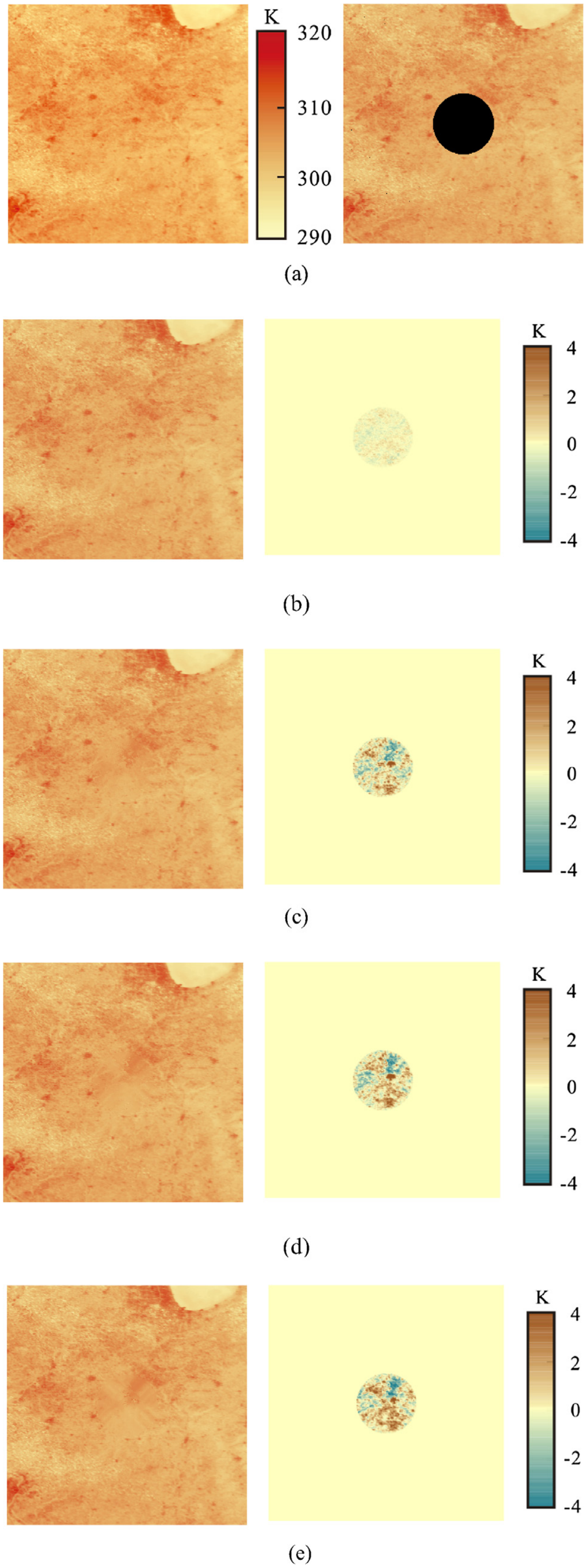

(a)

(b)

(c)

(d)

(e)

Fig. 8. An example of the simulated experiment: (a) the original LST of the study area (BON) acquired on June 30, 2010 and the simulated LST data degraded by an invalid region with 100 pixel diameter and the reference data acquired (b) 2, (c) 55, (d) 100, and (e) 151 days away and the corresponding error maps of reconstructed LST data.

4.2. Different acquisition dates of reference data

In addition to the spatial size of cloud-contaminated areas, the temporal interval between the contaminated LST and reference LST also has a significant impact on the reconstruction effect. To quantitatively assess this impact, a series of simulated experiments using reference data acquired on different dates were implemented, as an example shown in Fig. 8. Fig. 8(a) is the original LST image acquired on June 30, 2010, and the degraded LST image with an invalid area of 100 pixel diameter. Multiple reference LST images were used to reconstruct the invalid region and the results were compared. Fig. 8(b)–(e) are four reconstructed images and corresponding error maps using reference LST images acquired on July 2, May 6, October 8 and November 22, 2010, which are 2, 55, 100, 151 days away from the date of Fig. 8(a). It can be found that, as the time interval increases, the errors become more obvious. In Fig. 8(b), the invalid region was reconstructed using the reference LST acquired 2 days away from the original image, which means that the reference LST and the original LST were relatively close. As a result, the errors were all less than 1 K. As for Fig. 8 (c)–(e), the errors are much more significant than Fig. 8(b). Most of the errors range from 2 K to 4 K. The results indicated that, with a very close reference LST, the error of reconstructed LST may be insignificant, whereas using a temporally relatively far reference LST, the error may be much larger (e.g., 4 K).

To further illustrate the impact of different acquired dates on the reconstruction algorithm, all the experimental areas were tested with reference LST acquired on different dates, and the results are shown in Fig. 9. In Fig. 9(a), for all the regions, the correlation coefficients are higher than 0.9 with time intervals close to 0. As time intervals increase, the correlation coefficients dramatically change over most regions except DRA and TBL. In the worst case, the correlation coefficient is only 0.4. In Fig. 9(b) and (c), the AREs and MAEs reach the lowest values while the time interval is close to 0. Marked changes can be found as time intervals increase. However, the errors are particularly significant for TBL and DRA. It is because that in the reconstruction method, the relationship between LST and NDVI is used. However, the two regions are mainly covered by sand and rocks. Therefore, as for LST change, the vegetation is not the primary factor in most of the year. In this case, it was difficult to obtain accurate coefficients in Eq. (1). As a result, the errors were large but regular, which could lead to a high correlation coefficient and relatively high ARE and MAE. However, the AREs were still less than 1%, and most of the MAEs were less than 2 K. This means that the reconstruction method is still acceptable even the reference LST has large time intervals to the target LST image to be reconstructed.

4.3. Different vegetation indexes

In the former experiments, NDVI products were used in the multi-temporal reconstruction procedure. However, it is unclear whether other types of VI is effective in the method. In this part, the Enhanced Vegetation Index (EVI) and NDVI products were compared using data at GWN and TBL. Results are shown in Fig. 10. Generally, the reconstructed results using different VI products are very close. For both sites, the curves of correlation coefficients, ARE and MAE are nearly overlapped. Only slight differences can be found in Fig. 10(b) and (c), indicating that the NDVI has an insignificant advantage over the EVI in this algorithm.

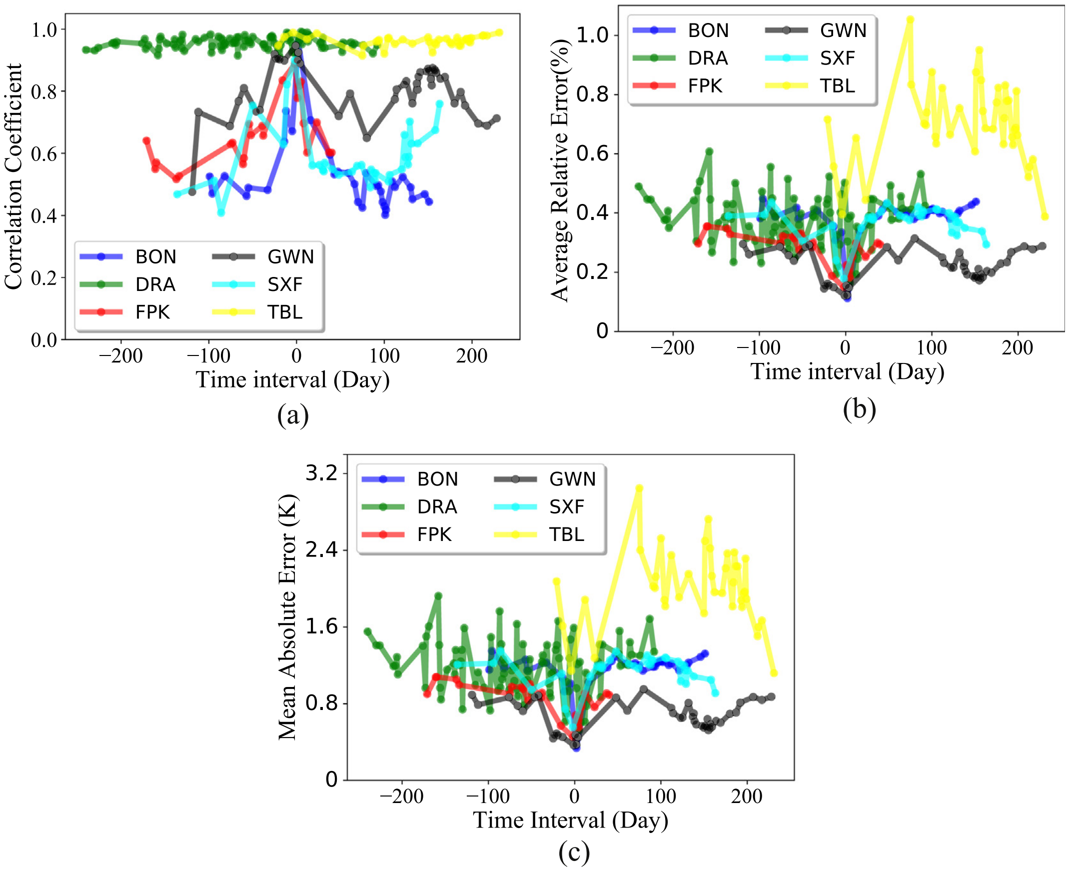

Fig. 9. (a) Correlation coefficients, (b) average relative errors, and (c) mean absolute errors of the 6 experimental regions with different temporal reference data.

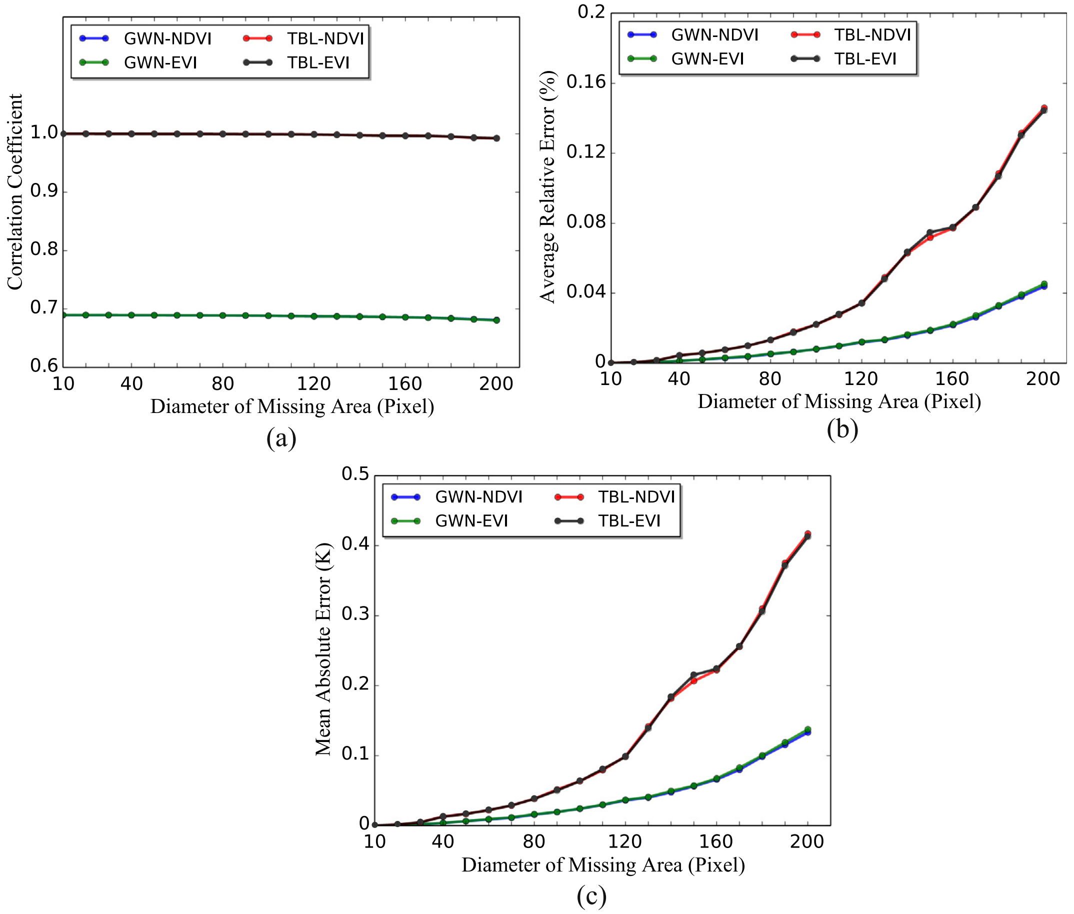

(a) (b) (c)

Fig. 10. (a) Correlation coefficients, (b) average relative errors, and (c) mean absolute errors of the GWN and TBL region with different vegetation indices (i.e., NDVI and EVI) as reference data.

4.4. Validation using SURFRAD data

In this part, to evaluate the SEB-based correction method, satellite-derived LST and reconstructed LST were compared with SURFRAD measured LST. In Fig. 11, scatterplots of the original satellite-derived LST against the ground measurements from 6 SURFRAD sites in 2010 are shown. In general, most of the satellite-based observations had excellent agreement with the ground measurements at the 6 sites, showing R^2 between 0.897 and 0.967, and the MAE between 2.213 K and 6.577 K. For the sites of BON, SXF and TBL, the MODIS LST was relatively unbiased, while in DRA and FPK, the MODIS LST was slightly overestimated. However, in GWN the satellite measurements were slightly underestimated. It can also be found that, for all the 6 sites, more than 140 days were contaminated by cloud. In particular for the FPK site, only 155 valid satellite observations were obtained during 2010, which means that this area was covered by cloud in more than half a year. It also demonstrated the importance of developing a LST reconstruction algorithm for practical applications.

Fig. 12 shows corresponding scatterplots of LST reconstructed by the multi-temporal method against the ground measurements at the 6 sites. However, in this experiment, not all the missing LST gaps were filled, because some LST images were totally invalid in the 400 by 400 pixels area. Therefore, there was no reference information that can be found in the experimental area. In this situation, the only solution was to enlarge the experimental area until sufficient reference pixels were included. But the extreme situation is not common. As for the reconstructed values, all of them had good agreement with the ground measurements. The R^2 ranged between 0.719 and 0.925, and the MAE ranged between 3.648 K and 6.692 K. Just as the experimental results shown in Figs. 7 and 9, at the sites of DRA and TBL, the accuracies were more likely to be affected by the land cover types. So the worst R^2 and MAE appeared at these two sites. It also demonstrated that, except site GWN, no obvious overestimation or underestimation can be found in the other 5 sites. This is because with the reference of NDVI, the bias in the MODIS LST can be filtered out.

In Fig. 13, scatterplots of corrected LST for cloudy conditions against ground-based measurements from 6 SURFRAD sites of 2010 are shown. Compared with Fig. 12, the results at sites BON, DRA, FPK and SXF were improved. All the R^2 increased by 0.02, and MAE decreased by 0.03–0.17 K. However, for site GWN, although R^2 increased from 0.802 to 0.807, the MAE increased from 6.692 to 6.797. This may be because the obvious underestimation in the reconstructed results of step 1 affected the correction. After correction, the reconstructed values decreased due to the accommodation of cloud cover, making the final results show more deviations from the ground measurements. In addition, for site TBL, R^2 remained 0.719, while the MAE increased from 5.890 to 5.915. The reason is that, as aforementioned, the land surface types made the algorithm difficult to search for stable similar information at this site. As a result, more errors were introduced to Eq. (24), making the result worse than the other sites.

It can be found that, in Figs. 12 and 13, the multi-temporal reconstructed LSTs are not obviously higher than the corrected and ground-measured LSTs. Since LST may be affected by many factors (such as precipitation, cloud cover time and soil thermal properties and moisture), the real LST under clouds may not be

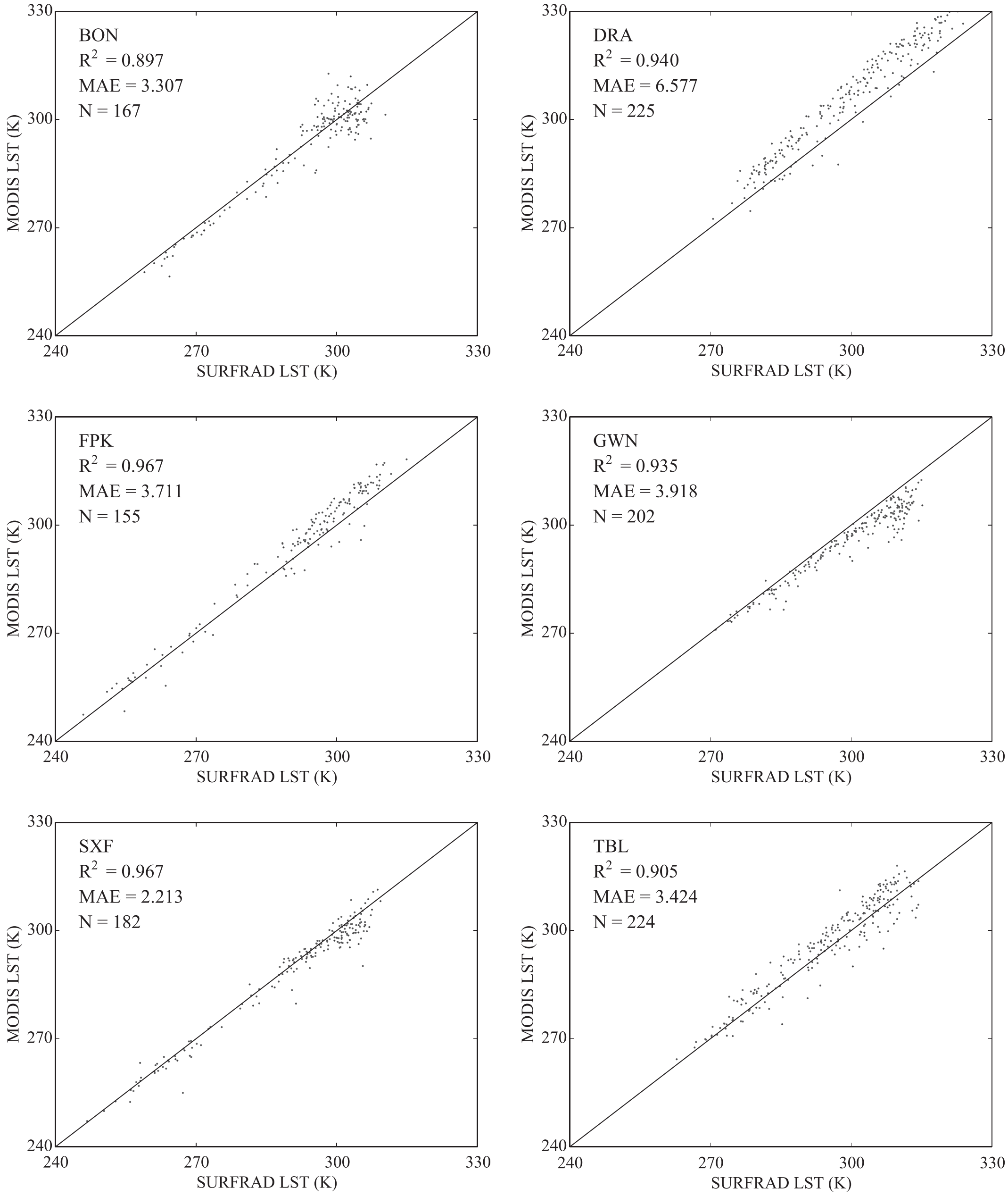

Fig. 11. Scatterplots of the ground-measured LST against the MODIS LST at 6 SURFRAD sites in 2010.

significantly lower than the clear-sky LST. The ground measurements of SURFRAD were used to explore the relationship between cloudy LSTs and clear-sky LSTs. All the ground measurements from neighboring cloudy and clear-sky days were collected. In order to exclude the effect of strong weather changes, the neighboring days with more than 20 K LST difference were removed. Then the remaining measurements were plotted as shown in Fig. 14. The cloudy LST and the clear-sky LST are rather close. The slope is 1.006 and the intercept is 0.725. It means that, compared with clear-sky LSTs, cloudy LSTs are statistically slightly smaller.

In Fig. 15, the histogram of errors of MODIS LST against SURFRAD sites measurements is shown. It can be found that the errors at the 6 sites were not normally distributed. The modal error is about 2 K. It means that most of the MODIS observed LST values were slightly underestimated. However, there was also a rising trend near −5 K, indicating that there were also a number of obvious overestimated LST values (mostly appeared over the DRA region as shown in Fig. 11). To further illustrate the reconstruction effect of the proposed method, errors of the two steps were calculated and shown in Fig. 16. Generally, the error distributions of the reconstructed LST were consistent with the original MODIS error distribution. In addition, like the original MODIS observations, the reconstructed values were also mostly underestimated. Fig. 16 shows that due to the correction of step 2, the overestimated values were significantly reduced, indicating the effectiveness of the SEB-based correction method.

4.5. Comparison to previous studies

The simulated experiments indicated that the proposed multi-temporal reconstruction algorithm is reliable for all the test regions. All the reconstructed areas were highly consistent with the original areas. The actual experiments also illustrated that the relationship between the reconstructed MODIS LST values and the ground measurements were quite similar with the relationship of observed MODIS LST values and the ground

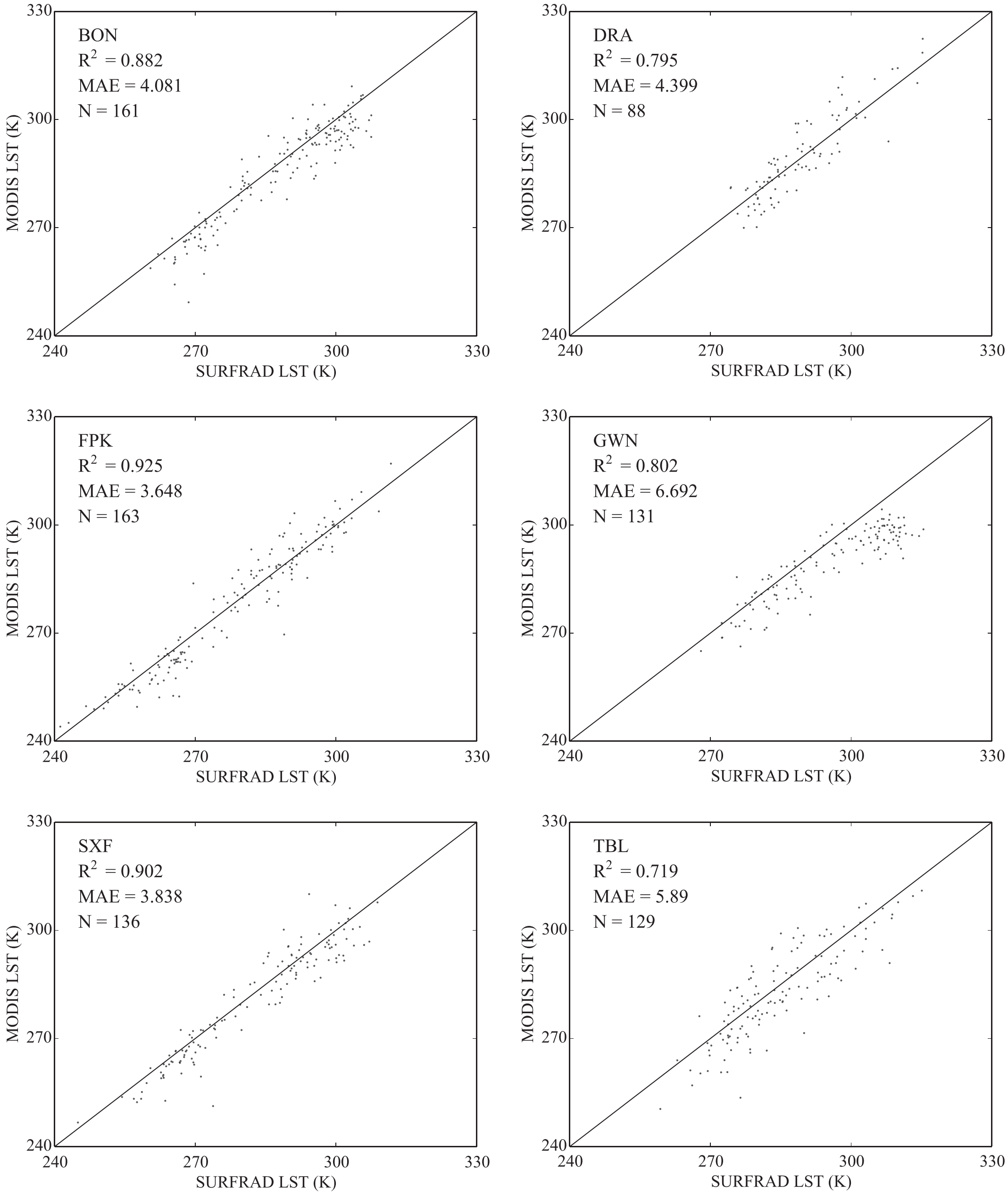

Fig. 12. Scatterplots of the ground-measured LST against the multi-temporal reconstructed MODIS LST at 6 SURFRAD sites in 2010.

measurements. Therefore, the proposed method can reconstruct cloud-contaminated LST accurately under different conditions. This new method also shows some advantages over the existing approaches. In Jin's paper (2000), the NP approach was tested by a climate model and showed an accuracy of 1–2 K at monthly mean pixel level resolution. Another NP-based case was validated with two ground sites in Africa and had root-mean-square errors (RMSE) of 5.55 and 5.11 K for the two sites, respectively (Lu et al., 2011). Yu et al. (2014) estimated cloud-contaminated MODIS LST products in the Hehei River basin and gave RMSE of 4.122 K. Compared to these published studies, the proposed method was evaluated under a range of locations, land cover types, and climatic conditions, showing MAEs about 3–6 K at different sites. This suggests that the new method is quite effective and stable in most cases.

5. Conclusion

Remote sensing LST products can offer accurate and large-scale LST with high temporal and spatial resolutions. However, data quality is often degraded by cloud. In this study, a two-step LST reconstruction method is proposed. Compared to existing methods, the new method can recover the real LST accurately without the requirement of ground-measured parameters. The effectiveness of the developed approach is demonstrated by a series of simulated and real experiments in two steps. Results indicate that the proposed method is relatively accurate and can be applied to different areas with varying land surface properties and climates. The usability of satellite-derived LST can therefore be significantly improved and numerous applications would also be benefited from this work.

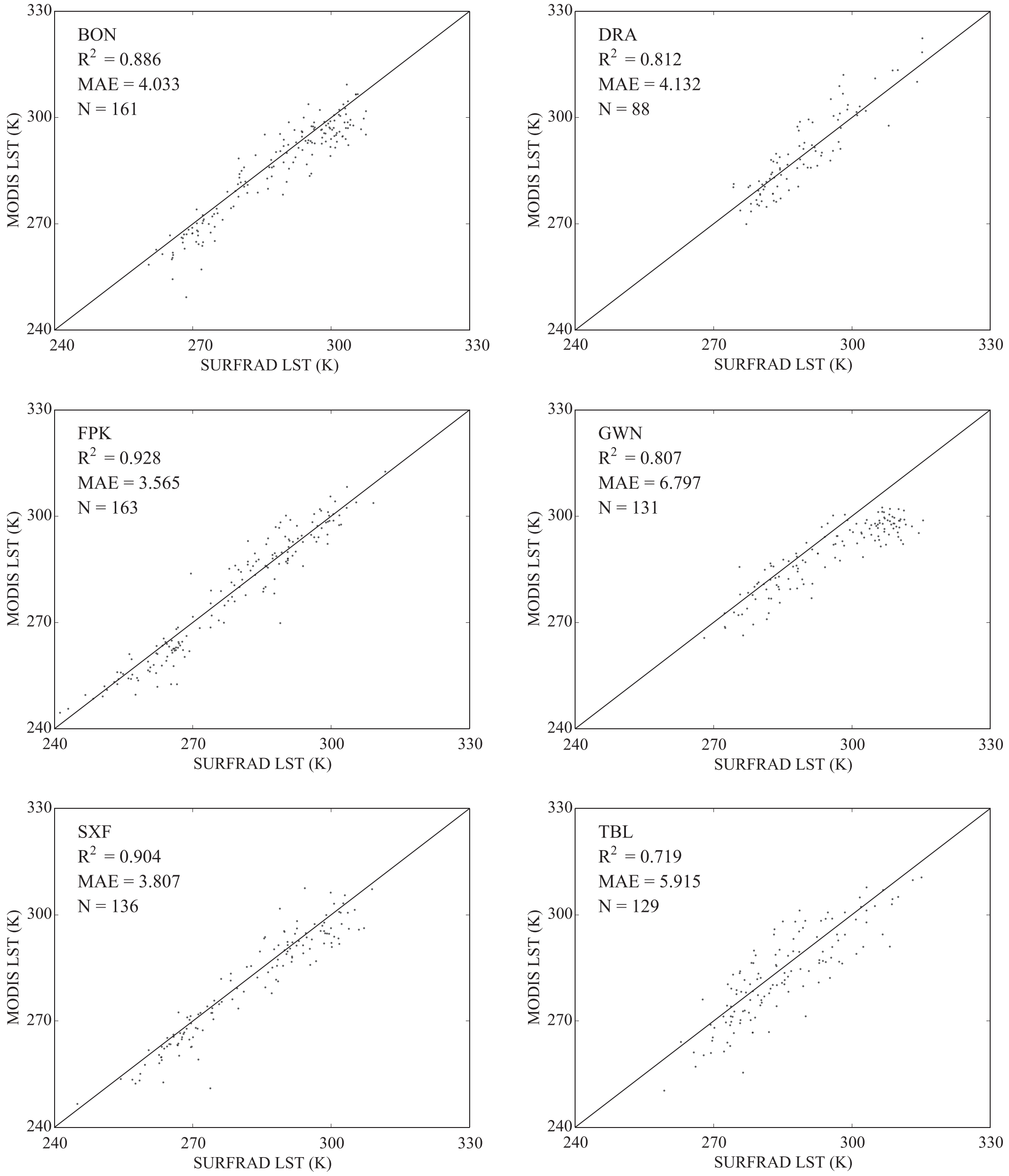

Fig. 13. Scatterplots of the ground-measured LST against the final reconstructed MODIS LST at 6 SURFRAD sites in 2010.

It should be noted that there is still room for further improving the proposed method. The 5 km resolution downward shortwave radiation data was resampled to 0.01°×0.01°. Since the resampling process cannot provide detailed information, it may introduce uncertainty to the reconstructed LST results. In addition, the correction in the second step may not be so useful for a small area, e.g., less than 100 MODIS pixels. Although the approach is effective and acceptable in all the experiments, we are also looking forward to a better downward shortwave radiation product with higher resolution in the future. The multi-temporal reconstruction method is developed based on the relationship between LST and NDVI. Therefore, larger errors can be found in the sandy and rocky regions such as TBL and DRA stations. To make the multi-temporal reconstruction method more robust, a multi-factor relationship can be considered in further work. In addition, in the SEB-based correction method, the net longwave radiation, sensible heat and latent heat flux are approximated with net shortwave radiation for simplicity, since there are no simple and reliable datasets of those variables at the 1 km resolution. As spatiotemporal

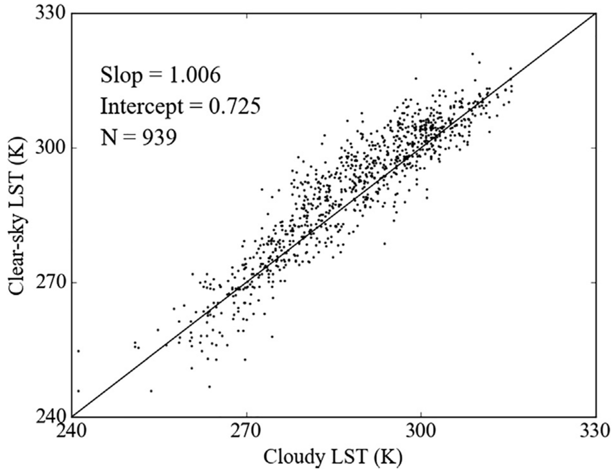

Fig. 14. Scatter plot of neighboring cloudy and clear-sky LST from the 6 ground sites.

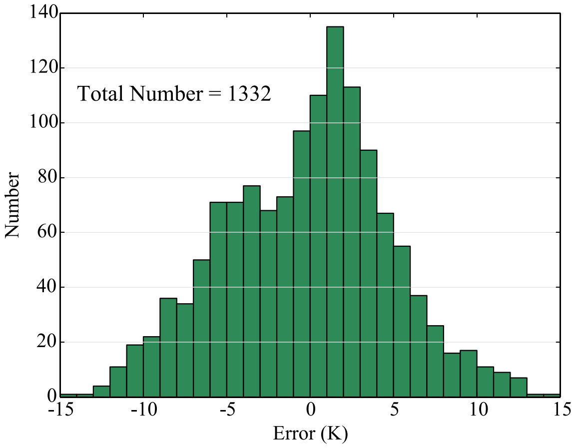

Fig. 15. Histogram of errors (ground-measured LST minus the observed MODIS LST) at 6 SURFRAD sites in 2010.

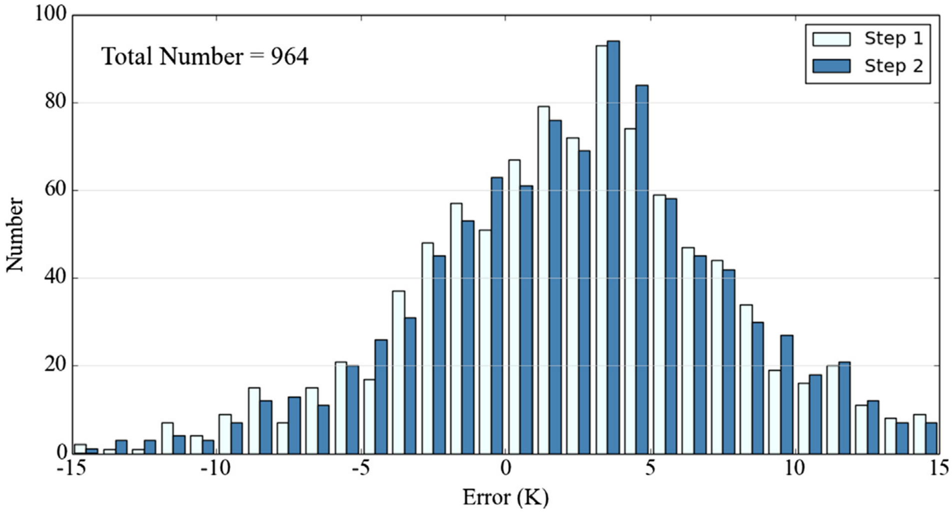

Fig. 16. Histogram of errors (ground-measured LST minus the MODIS LST reconstructed by two steps, respectively) at 6 SURFRAD sites in 2010.

resolution and reliability of radiation products evolve, the developed framework can be better applied.

Acknowledgments

This study was financially supported by the National Natural Science Foundation of China (Grant Nos. 91547210, 41601359, 91437214, and 51579128). Additional support was from the foundation of the State Key Laboratory of Hydroscience and Engineering of Tsinghua University under grant 2016-KY-03. Editors and three anonymous reviewers' comments which are highly valuable for improving this manuscript are appreciated.

References

Amiri, R., Weng, Q., Alimohammadi, A., Alavipanah, S.K., 2009. Spatial–temporal dynamics of land surface temperature in relation to fractional vegetation cover and land use/cover in the Tabriz urban area, Iran. Remote Sens. Environ. 113 (12), 2606–2617.

Anderson, M.C., Norman, J.M., Kustas, W.P., Houborg, R., Starks, P.J., Agam, N., 2008. A thermal-based remote sensing technique for routine mapping of land-surface carbon, water and energy fluxes from field to regional scales. Remote Sens. Environ. 112, 4227–4241.

Arnfield, A.J., 2003. Two decades of urban climate research: a review of turbulence, exchanges of energy and water, and the urban heat island. Int. J. Climatol. 23, 1–26.

Augustine, J.A., Deluisi, J.J., Long, C.N., 2010. Surfrad-a national surface radiation budget network for atmospheric research. Bull. Am. Meteorol. Soc. 81 (10), 2341–2357.

Cai, D., Guo, N., Li, C., 2009. Interpolation of air temperature based on DEM over eastern region of Gansu. J. Arid Meteorol. 27 (1), 10–17.

Cleveland, W.S., Devlin, S.J., 1988. Locally weighted regression: an approach to regression analysis by local fitting. J. Am. Stat. Assoc. 83 (403), 596–610.

Dousset, B., Gourmelon, F., 2003. Satellite multi-sensor data analysis of urban surface temperatures and landcover. ISPRS J. Photogramm. Remote Sens. 58 (1), 43–54.

Estoque, R.C., Murayama, Y., 2017. Monitoring surface urban heat island formation in a tropical mountain city using Landsat data (1987–2015). ISPRS J. Photogramm. Remote Sens. 133, 18–29.

Hansen, J., Ruedy, R., Sato, M., Lo, K., 2010. Global surface temperature change. Rev. Geophys. 48.

Jin, M.L., 2000. Interpolation of surface radiative temperature measured from polar orbiting satellites to a diurnal cycle. 2. Cloudy-pixel treatment. J. Geophys. Res. – Atmos. 105, 4061–4076.

Jin, M.L., Dickinson, R.E., 2000. A generalized algorithm for retrieving cloudy sky skin temperature from satellite thermal infrared radiances. J. Geophys. Res. – Atmos. 105, 27037–27047.

Jin, M.L., Dickinson, R.E., 2010. Land surface skin temperature climatology: benefitting from the strengths of satellite observations. Environ. Res. Lett. 5.

Jimenez-Munoz, J.C., Sobrino, J.A., 2003. A generalized single-channel method for retrieving land surface temperature from remote sensing data. J. Geophys. Res. – Atmos. 108.

Ke, L., Wang, Z., Song, C., Lu, Z., 2011. Reconstruction of MODIS LST time series and comparison with land surface temperature (T) among observation stations in the northeast Qinghai-Tibet Plateau. Prog. Geogr. 30 (7), 819–826.

Kustas, W., Anderson, M., 2009. Advances in thermal infrared remote sensing for land surface modeling. Agric. For. Meteorol. 149, 2071–2081.

Li, S.M., Yu, Y.Y., Sun, D.L., Tarpley, D., Zhan, X.W., Chiu, L., 2014. Evaluation of 10 year AQUA/MODIS land surface temperature with SURFRAD observations. Int. J. Remote Sens. 35, 830–856.

Li, Z.L., Tang, B.H., Wu, H., Ren, H.Z., Yan, G.J., Wan, Z.M., Trigo, I.F., Sobrino, J.A., 2013. Satellite-derived land surface temperature: Current status and perspectives. Remote Sens. Environ. 131, 14–37.

Liang, S., Zhao, X., Liu, S., Yuan, W., Cheng, X., Xiao, Z., Qu, Y., 2013. A long-term Global LAnd Surface Satellite (GLASS) data-set for environmental studies. Int. J. Digital Earth 6 (sup1), 5–33.

Lu, L., Venus, V., Skidmore, A., Wang, T.J., Luo, G.P., 2011. Estimating land-surface temperature under clouds using MSG/SEVIRI observations. Int. J. Appl. Earth Obs. Geoinf. 13, 265–276.

Neteler, M., 2010. Estimating daily land surface temperatures in mountainous environments by reconstructed MODIS LST data. Remote Sens. 2, 333–351.

Niclòs, R., Pérez-Planells, L., Coll, C., Valiente, J.A., Valor, E., 2018. Evaluation of the S-NPP VIIRS land surface temperature product using ground data acquired by an autonomous system at a rice paddy. ISPRS J. Photogramm. Remote Sens. 135, 1–12.

Qin, Z., Karnieli, A., Berliner, P., 2001. A mono-window algorithm for retrieving land surface temperature from Landsat TM data and its application to the Israel-Egypt border region. Int. J. Remote Sens. 22, 3719–3746.

Rajasekar, U., Weng, Q., 2009. Urban heat island monitoring and analysis using a non-parametric model: a case study of Indianapolis. ISPRS J. Photogramm. Remote Sens. 64 (1), 86–96.

Schultz, P.A., Halpert, M.S., 1995. Global analysis of the relationships among a vegetation index, precipitation and land-surface temperature. Int. J. Remote Sens. 16, 2755–2777.

Shen, H.F., Huang, L.W., Zhang, L.P., Wu, P.H., Zeng, C., 2016. Long-term and fine-scale satellite monitoring of the urban heat island effect by the fusion of multi-temporal and multi-sensor remote sensed data: a 26-year case study of the city of Wuhan in China. Remote Sens. Environ. 172, 109–125.

Shen, H., Zeng, C., Zhang, L., 2011. Recovering reflectance of AQUA MODIS band 6 based on within-class local fitting. IEEE J. Sel. Top. Appl. Earth Obs. Remote Sens. 4, 185–192.

Shuai, T., Zhang, X., Wang, S.D., Zhang, L.F., Shang, K., Chen, X.P., Wang, J.N., 2014. A spectral angle distance-weighting reconstruction method for filled pixels of the MODIS land surface temperature product. IEEE Geosci. Remote Sens. Lett. 11, 1514–1518.

Wan, Z.M., Dozier, J., 1996. A generalized split-window algorithm for retrieving land-surface temperature from space. IEEE Trans. Geosci. Remote Sens. 34, 892–905.

Wang, K.C., Liang, S.L., 2009. Evaluation of ASTER and MODIS land surface temperature and emissivity products using long-term surface longwave radiation observations at SURFRAD sites. Remote Sens. Environ. 113, 1556–1565.

Wang, K.C., Wan, Z.M., Wang, P.C., Sparrow, M., Liu, J.M., Zhou, X.J., Haginoya, S., 2005. Estimation of surface long wave radiation and broadband emissivity using Moderate Resolution Imaging Spectroradiometer (MODIS) land surface temperature/emissivity products. J. Geophys. Res. – Atmos. 110.

Weng, Q.H., 2009. Thermal infrared remote sensing for urban climate and environmental studies: methods, applications, and trends. ISPRS J. Photogramm. Remote Sens. 64 (4), 335–344.

Weng, Q.H., Fu, P., 2014. Modeling annual parameters of clear-sky land surface temperature variations and evaluating the impact of cloud cover using time series of Landsat TIR data. Remote Sens. Environ. 140, 267–278.

Wu, P.H., Shen, H.F., Ai, T.H., Liu, Y.L., 2013. Land-surface temperature retrieval at high spatial and temporal resolutions based on multi-sensor fusion. Int. J. Digital Earth 6, 113–133.

Wu, P.H., Shen, H.F., Zhang, L.P., Göttsche, F.-M., 2015. Integrated fusion of multi-scale polar-orbiting and geostationary satellite observations for the mapping of high spatial and temporal resolution land surface temperature. Remote Sens. Environ. 156, 169–181.

Xu, Y.M., Shen, Y., 2013. Reconstruction of the land surface temperature time series using harmonic analysis. Comput. Geosci. 61, 126–132.

Yoo, C., Im, J., Park, S., Quackenbush, L.J., 2018. Estimation of daily maximum and minimum air temperatures in urban landscapes using MODIS time series satellite data. ISPRS J. Photogramm. Remote Sens. 137, 149–162.

Yu, W.P., Ma, M.G., Wang, X.F., Tan, J.L., 2014. Estimating the land-surface temperature of pixels covered by clouds in MODIS products. J. Appl. Remote Sens. 8.

Zeng, C., Shen, H.F., Zhang, L.P., 2013. Recovering missing pixels for Landsat ETM+ SLC-off imagery using multi-temporal regression analysis and a regularization method. Remote Sens. Environ. 131, 182–194.

Zeng, C., Shen, H.F., Zhong, M.L., Zhang, L.P., Wu, P.H., 2015. Reconstructing MODIS LST based on multitemporal classification and robust regression. IEEE Geosci. Remote Sens. Lett. 12, 512–516.

Zhang, X.T., Liang, S.L., Zhou, G.Q., Wu, H.R., Zhao, X., 2014. Generating Global LAnd Surface Satellite incident shortwave radiation and photosynthetically active radiation products from multiple satellite data. Remote Sens. Environ. 152, 318–332.

Zhang, X.Y., Li, P.J., 2018. A temperature and vegetation adjusted NTL urban index for urban area mapping and analysis. ISPRS J. Photogramm. Remote Sens. 135, 93–111.